

# Stress and strain analysis and induced seismicity in geological gas storage (Yela, Spain)

Raúl Pérez-López<sup>a,\*</sup>, Adrià Ramos<sup>a</sup>, Jorge L. Giner-Robles<sup>b</sup>

<sup>a</sup> Instituto Geológico y Minero de España (IGME – CSIC), C/Ríos Rosas 23, Madrid, 28400, Spain

<sup>b</sup> Universidad Autónoma de Madrid, Spain

## ARTICLE INFO

### Keywords:

Stress-strain

Geologic gas storage

Induced seismicity

Fault kinematics

## ABSTRACT

Geologic gas storage is a sustainable strategy to store energy in underground reservoirs in order to be used under demand. Injection and withdrawal gas operations could trigger induced seismicity according to the tectonic constraints of the reservoir. The study of the active stress/strain fields shows the properties of the fault patterns that can be involved in induced seismicity. In our work, we have determined the strain/stress field in the Yela underground gas storage, an Upper Cretaceous carbonate reservoir located in central Spain. Slickensides on fault planes were measured from Cretaceous, Miocene and Quaternary rocks. Results show a strain field with  $\epsilon_y$  (maximum horizontal shortening) oriented NW-SE. This field was compressional during the early Miocene, switching off to extensional from late Miocene to present-day. Our results suggest that NNW-SSE and NW-SE oriented faults could act as an effective pathway for gas leakage and prone to trigger induced seismicity. Moreover, 141 small earthquakes ( $M_{\max}$  2.3) were recorded during underground operations in Yela. Peaks of earthquakes appear seasonally from November to February, in coincidence with the injection operations prior to the winter withdrawal. Working at its maximum gas storage volume, earthquake peaks decreased in intensity and magnitude from 2017 to 2021, and show a time lag of 3 months from the month of maximum volume injection to the earthquake occurrence.

## 1. Introduction

Microscopic kinematic analysis is a common technique in structural geology to determine paleostress strain/stress fields from outcrops (e.g. Etchecopar et al., 1981; Armijo et al., 1982; Ramsay and Huber, 1983, 1987; Reches, 1987; Angelier, 1990; Capote et al., 1990), which has evolved including complex fractal geometries (Pérez-López et al., 2005), and has led to the development of numerical models beyond the classical view of the Anderson's fracture model (Žalohar and Vrabec, 2010). However, the paleostress reconstruction is constrained from the geological structures, which are commonly folded and faulted, determining the spatial distribution of the fault-slip data (Amrouch et al., 2010). Microstructural analysis can be applied in geologic gas storages, complementing it with other strain/strain methods, such as earthquake focal mechanism solutions or calcite twin analysis (e.g. Lacombe, 2007).

Underground geologic gas storage sites are conceived as long-lived facilities, while geophysical monitoring is an essential practice for keeping industrial operations safe in the long-term future. One of the main concerns in underground gas storages is the possibility of

triggering earthquakes. Preventing induced earthquakes during the injection/withdrawal gas operations needs a knowledge of several geological parameters such as existing fault and fracture networks, present-day stress and pressure conditions, geomechanical constraints regarding rock failure, total gas volume stored, and daily gas flow of the injected gas, among others.

The classical microstructural analysis of striation measurements on fault planes provides an economical and accessible method for estimating the paleostress/-strain fields of geological reservoirs (Pérez-López et al., 2020), acting as a key parameter to understand the induced seismicity potential. Among others, the Right-Dihedral and the Slip Model methods (Pérez-López et al., 2020) can be applied to identify the strain field, whereas the stress field can be determined from the analysis of earthquake focal mechanism solutions. Hence, the coefficient of reactivation for fault sets affecting the reservoir can be determined, according to their agreement with the strain field, and their role in the reservoir permeability and as leakage pathways.

The geologic gas storage of Yela (Guadalajara, Central Spain, Fig. 1) is operating since 2012. It is a strategic storage facility for natural gas,

\* Corresponding author.

E-mail address: [r.perez@igme.es](mailto:r.perez@igme.es) (R. Pérez-López).

<https://doi.org/10.1016/j.jsg.2022.104662>

Received 17 September 2021; Received in revised form 20 April 2022; Accepted 14 June 2022

Available online 25 June 2022

0191-8141/© 2022 The Authors. Published by Elsevier Ltd. This is an open access article under the CC BY-NC-ND license (<http://creativecommons.org/licenses/by-nc-nd/4.0/>).

which is stored and withdrawn according to the seasonal demand of the Spanish energy market. The Yela storage site is located in an intraplate tectonic zone, where no relevant earthquakes were recorded before the gas operations started. The Spanish Seismic Network, operated by the Geographical Institute of Spain ([www.ign.es](http://www.ign.es)), have been recording and collecting earthquakes from 1985 with a magnitude of completeness of  $M_c = 1.5$ , where  $M_c$  is the minimum magnitude above which all earthquakes within the studied area are reliably. A set of micro earthquakes ( $n = 141$ ;  $M < 2.3$ ) have been triggered since the starting of the injection/extraction operations in 2012 in the influence area of the injection operations (a few kilometres).

On the other hand, the regional tectonic stress field in Yela was extrapolated from a few data of small-sized ( $3 > M > 4.5$ ) intraplate earthquakes located in the vicinity (50 km away, [Herraiz et al., 2000](#); [Giner-Robles et al., 2012](#)). More extensive studies of the strain/stress field could help to understand the injected fluid interaction with the recorded microseismicity, the fault reactivation, and therefore, prevent a future seismic occurrence. Moreover, the strain/stress determination facilitates earthquake hazard information applicable to other sub-surface injection operations, such as oil and gas production or  $\text{CO}_2$  storages ([Pérez-López et al., 2020](#)).

The aim of this work is to determine the potential induced seismicity at the Yela gas storage site, the role of the strain/stress field, and those fault sets prone to move and act as leakage pathways. In this way, we have analysed the microscopic kinematic data from fault-slip slicken-sides and the macroscopic and regional strain/stress field derived from earthquake focal mechanism solutions. In total, 24 outcrops with 375 slip data were measured and analysed. We have estimated the potential fault sets reactivated under the current stress/strain field, and their role

as leaking pathways for the injected gas. Finally, we have studied the induced seismicity during the injection/withdrawal operations at Yela site. Our results show small clusters of induced earthquakes during the winter injection operations, lasting from November to February. These seismic clusters appeared for the first time in 2012 coinciding with the starting gas operations, and appeared annually until 2021. Although the gas storage facility is working at its maximum capacity, the recorded induced earthquake activities have decreased in frequency and magnitude over the last period from 2017 to 2021.

## 2. Geological setting

The underground natural gas storage facility of Yela is located in the northeastern extent of the Madrid Basin, central Spain ([Fig. 1a](#)). The Cenozoic Madrid Basin is bordered by the intraplate mountain range Central System to the north and the fold and thrust belt Iberian Chain to the northeast developed during the Cenozoic ([Fig. 1a](#)). The basin was filled and deformed during Cenozoic times due to the folding of the Iberian Peninsula lithosphere related to the convergence between Iberia and Eurasian plates ([Cloetingh et al., 2002](#)). The Central System consists of intraplate thick-skinned basement pop-up oriented E-W to NE-SW, of Oligocene-lower Miocene in age, while some structures were reactivated during the upper Miocene-Pliocene ([de Vicente et al., 2007](#)). However, to the NE, the compressional deformation is distributed by syntectonic fault-propagation folds ([de Vicente and Muñoz-Martín, 2013](#)), induced by SE-directed basement-involved thrust faults ([Fig. 1c](#)). To the east, the Madrid Basin is connected with the Iberian Chain, which consists of a NW-SE intraplate deformation belt, formed during the Cenozoic inversion of the Iberian Basin (e.g. [Guimerà et al., 2004](#)). The occurrence of

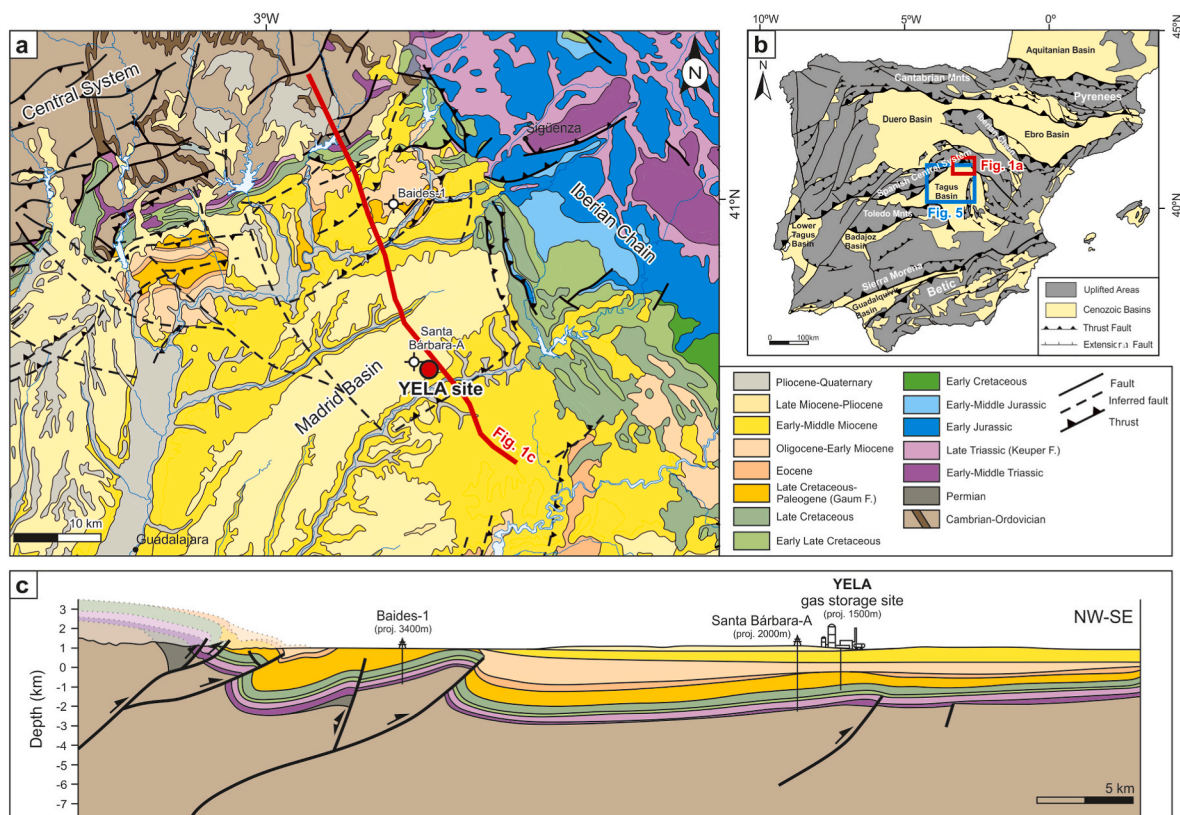


**Fig. 1.** a) Detailed geological map of the NE portion of the Madrid Basin, which is limited by the Central System the NW and by the Iberian Chain to the NE. Modified after [Rodríguez et al. \(2015\)](#). Notice the location of the Yela geologic gas storage (natural gas) site (red dot), the exploration wells available in the study area and the cross-section illustrated in [Fig. 1c](#) (red line). b) Schematic map showing the location of Cenozoic structures of Iberia and the study area (red rectangle), modified after [Ramos et al. \(2017\)](#). c) Cross section running from the Central System to the central part of the Madrid Basin, showing the SE-verging involved thrusts controlling the Cenozoic deposition (modified after [de Vicente and Muñoz-Martín, 2013](#)). (For interpretation of the references to colour in this figure legend, the reader is referred to the Web version of this article.)

NW-SE folds is related to basement-involved thrusts and positive flower structures, partially covered by the Cenozoic sediments of the Madrid Basin (Fig. 1c).

The Cenozoic Madrid Basin lies was deposited on a sedimentary cover consisting of clastic Permian-Triassic succession followed by Middle to Upper Triassic carbonates including evaporitic sequences. The Jurassic to Lower Cretaceous sequences are missing in the area. This omission is related to the no deposition beyond the current mountain ranges, which in turn were Mesozoic rift areas. The sedimentary record of the Madrid Basin is rather continuous from the Late Cretaceous to the late Miocene, deposited in continental environments and showing different lithology such as sandstones, claystones, marls, limestones or gypsum.

The Oligocene-Lower Miocene sedimentary infilling coincide with the maximum tectonic activity at the basin borders, which produced progressive discordances associated with folds of different orientation (de Vicente and Muñoz-Martín, 2013 and references therein). The main tectonic structure in the area consists of a large SE-directed crustal-scale thrust, which puts in contact the southern margin of the Central System with the Madrid Basin (Fig. 1b). This regional structure is represented by a basement flexure determined by a NE-trending axis, which is related with instrumental seismicity of magnitude maximum as  $M = 4.2$  (Escopete earthquake, 7th June of 2007), and shallow earthquakes ( $<10$  km) with normal focal mechanisms (Giner-Robles et al., 2012). This basement flexure is in agreement with the regional stress/strain tensor defined by Herraiz et al. (2000).

The geologic gas storage of Yela is an underground natural gas and strategic reservoir. This reservoir consists of a saline aquifer in a carbonate succession, 8 km long with a NE-SW trend, and covering an area of 25 km<sup>2</sup>. The depth of the reservoir ranges between 2,300 and 2,550 m, and the total storage volume is ca 6.25 km<sup>3</sup>. The lithology of the reservoir is represented by the “Santa Bárbara” formation, which consists of Cretaceous carbonates, mainly dolostones (Conian-Santonian) affected by a diffuse fracture network, overlain and sealed by evaporitic facies. The structural trap consists of a NE-SW fault-propagation fold (Fig. 1), accommodated on a SE-directed thrust, NE-SW oriented (Figs. 1a and 4).

### 3. Methods and rationale

Stress and strain fields play a relevant role in the permeability of underground gas reservoirs. The reservoir is affected by the tectonic field, especially when increasing gas pressure that might promote leakage (Pérez-López et al., 2020). The estimation of 3D fracture networks relative to the active stress and strain fields within the reservoir allows to prevent the induced seismicity related to fluid injection or withdrawal by deploying seismic arrays.

The application of the common techniques of paleostress analysis in field outcrops (i.e. Etchecopar et al., 1981; Reches, 1983; Angelier, 1990; Delvaux and Sperner, 2003), provides the local strain/stress field evolution through time in a reservoir (Pérez-López et al., 2020). These techniques estimate the stress/strain fields by measuring grooves and slickensides on fault planes (Reches, 1983), among other displacement indicators. The strain tensor is an ellipsoid defined by the orientation of the principal axes, which can be projected in the plane,  $e_y$  = maximum horizontal shortening,  $e_x$  = minimum horizontal shortening, and  $e_z$  = vertical strain, and the shape of the ellipsoid. This method assumes that the fault slip-vector defines a common strain tensor within a homogeneous tectonic setting. We assume that the strain field is homogeneous in space and time and the number of faults activated is greater than 5 (orthorhombic tensor), while the slip vector is parallel to the maximum shear stress ( $\tau$ ). Here we have used the horizontal shortening, a 2D projection of the strain tensor (Ramsay and Huber, 1983) to define the strain tensor affecting the geologic gas storage. In this work, we have performed an analysis of the fault kinematics, by measuring slickensides on fault planes (dip, dip-direction, and rake), in several

outcrops in the surroundings of the reservoir (20 km away from the Yela gas reservoir). The paleostress inversion method has been applied in fault planes present in Cretaceous and Neogene successions (late Miocene to present-day).

#### 3.1. The right-dihedral model for paleostress analysis

Ramsay (1967) pointed out that strain is mainly a matter of geometry. The Right-Dihedral method (RD) is a semi-quantitative method based on the overlapping of compressional and extensional zones by using a stereographic plot. The result is an interferogram plot, which defines the tectonic strain-regime. This method provides robust results for conjugate fault sets with different dip values for the same strain tensor, drawing different plot symmetry (dihedron) according to the type of the strain tensor (extensional, compressional and strike-slip). This method was originally defined by Angelier and Mechler (1977), as a geometric method, adjusting the measured fault-slip data (slickensides) in agreement with the theoretical models for extension and compressive fault-slip. We can constrain the regions of maximum compression and extension related to the strain regime in the final dihedron.

#### 3.2. The Slip Model for the paleostress analysis

The Slip Model (SM) is based on the Navier-Coulomb fracturing criteria (Reches, 1983), taking the Anderson model solution (Anderson, 1951; Simpson, 1997). The Anderson model is based on the quantitative parameters of the tensor shape parameter with the internal frictional angle for rocks ( $\phi$ , Capote et al., 1991). This model shows the relationships between the tensor shape,  $\phi$  and the direction cosines for the striation on the fault plane (Capote et al., 1991).

#### 3.3. The $K'$ strain diagram

The  $K'$ -diagram (Kaverina et al., 1996; Álvarez-Gómez, 2019) is a triangular representation based on the fault-slip, which discriminates between strike-slip and dip-slip tectonic patterns. The triangular graph is based on the equal-area representation of the main axes, T, N or B and P (T: tensile; N or B: neutral; P: pressure axes). This method was originally performed for earthquake focal mechanism solutions by using the focal parameter, nodal plane and rake (Kaverina et al., 1996). Pérez-López et al. (2020) introduced the use of the strain tensor shape combined with the  $K'$ -diagram, and divided the diagram in 7 different zones according to the type of fault: (1) pure normal, (2) pure reverse and (3) pure strike-slip, (4) reverse strike-slip, (5) strike-slip with reverse component, (6) normal strike-slip, and (7) strike-slip faults with normal component. Strike-slip faults are defined by small pitch values ( $p < 25^\circ$ ), with dip close to a vertical plane ( $\beta > 75^\circ$ ). High pitch values ( $p > 60^\circ$ ) are related to normal or/reverse fault-slip vectors. Extensional faults show  $e_y$  in vertical whereas compressional faults show  $e_y$  in a horizontal plane. The advantage of using this diagram is the direct assignation of the fault type and the tectonic regime, as well as the strain axes relationship. Hence, the  $K'$ -diagram classifies the type of fault according to the strain tensor.

#### 3.4. Paleostress analysis

Pérez-López et al. (2020) carried out a first approach to the application of the paleostress analysis in the surroundings of geologic carbon storage (GCS) in Hontomín (central Spain). They performed the analysis in a 20 km radius circle, centered in the Hontomín reservoir. This circle size was estimated taking into account active faulting with the capacity of triggering earthquakes with magnitudes up to  $M 6$ , which show a surface rupture of tens of kilometers length (Wells and Coppersmith, 1994). Verdon et al. (2015) pointed out that the maximum distance of induced earthquakes for fluid injection is 20 km, according to the



empirical evidence from plotting epicenters and injection wells. Larger distances could not be related to the stress/strain regime within the reservoir, except for the case of large geological structures affected by static stress changes (folds, master faults, etc.).

The presence of master faults (triggering earthquakes of magnitude  $\geq 6$ ) inside the 20 km radius circle implicates that the regional tectonic stress field determines the strain accumulation into the reservoir. Additionally, the presence of master faults could increase the occurrence of micro-earthquakes, due to the presence of secondary faults prone to trigger earthquakes by their normal seismic cycle (Scholz, 2018).

To compare the kinematics results from the analysis of micro fault-slip data with the macro analysis, we have studied the regional earthquake focal mechanism solutions (Giner-Robles et al., 2012). Hence, the fault plane reactivation have been studied by using the Mohr-Coulomb failure criterion (Pan et al., 2016), from the focal mechanism solutions of regional earthquakes (50 km around the gas energy storage facilities, [www.ign.es](http://www.ign.es), last access June 2021).

We have obtained the strain field ( $e_y$  main direction and  $K'$ ), from the Right-Dihedral and Slip Model applying fault-slip data (kinematics) and focal mechanism solutions for regional earthquakes. We have used the Win-tensor software (Delvaux and Sperner, 2003) to obtain the stress tensor from the focal mechanism solutions to be compared with the

strain results of earthquakes and faults, and the slip-tendency analysis from the Mohr circle.

In this work, we assumed that the orientation of the stress axis 2D horizontal projection,  $S_{Hmax}$  is parallel to the orientation of the strain axes 2D horizontal projection, and for instantaneous strain cases. Hence,  $e_y$ , the minimum horizontal stress axis,  $S_{Hmin}$ , is parallel to the minimum horizontal strain axis,  $e_x$ . This assumption allows us to estimate the plane projection of the stress trajectories ( $S_{Hmax}$  and  $S_{Hmin}$ ) from the  $e_y$  SM results.

#### 4. Results

A total of 375 kinematic fault-slip data in 24 outcrops were collected within the 20 km radius circle (results in Fig. 2, geographical location in Fig. 3.), mainly slickenside lineaments with sense of the movement developed on calcite/dolomite fault microplanes (cm-sized). Data are summarized in the supplementary material (excel file). The magnetic declination was lesser than  $1^\circ$ , and we assumed a compass error by field measuring of  $\pm 5^\circ$ . Outcrops with a number of data lesser than 5 measurements have been removed from the analysis since the RD and SD methods are not able to estimate the slip solutions with 4 or less number of data. Stratigraphic ages comprise from Cretaceous, early Miocene,

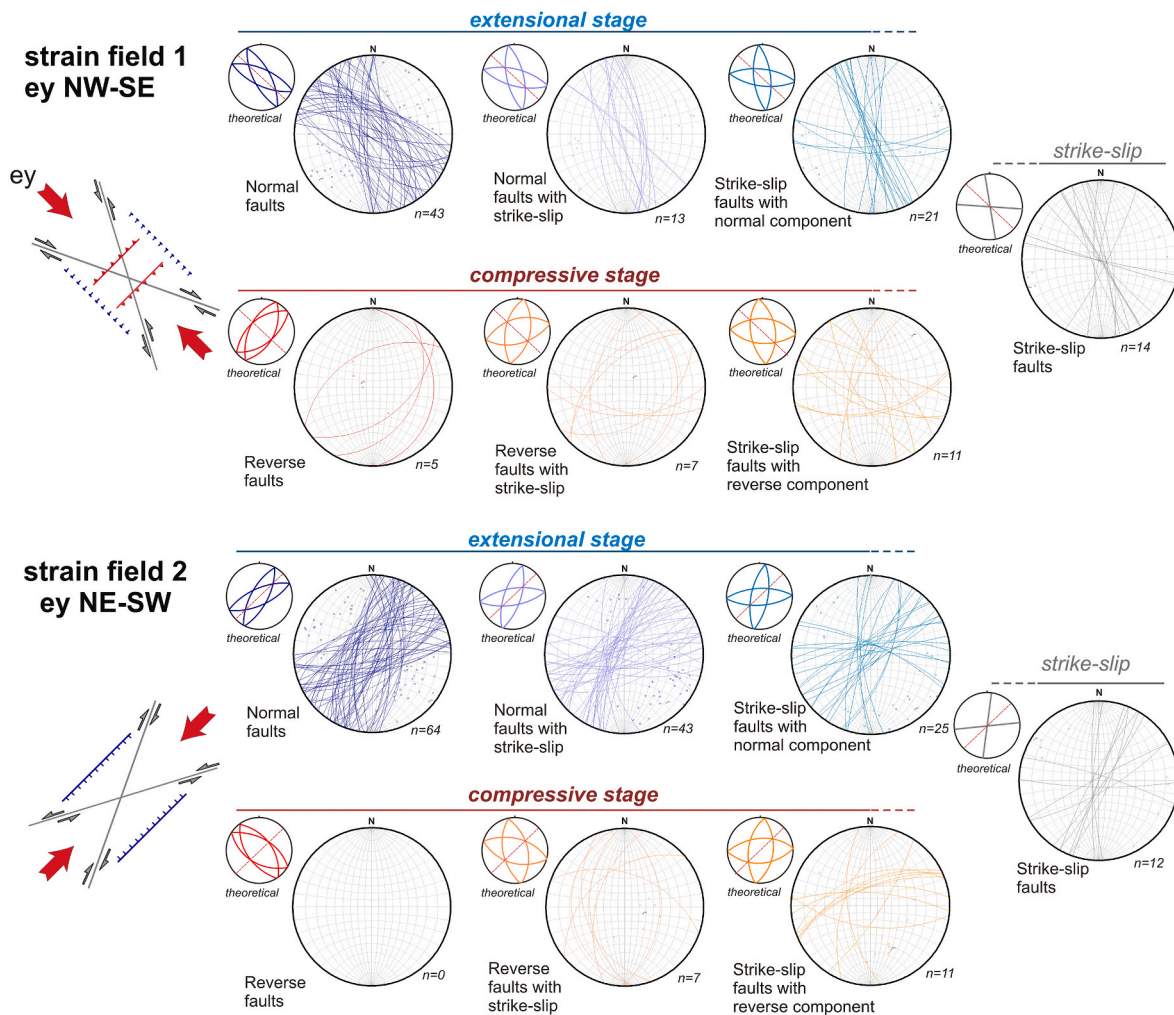


**Fig. 2.** Tectonic strain fields defined from the Right-Dihedral and Slip-Model within a 20 km radius circle around the Yela geological gas storage. The strain field 1 is defined by  $e_y$  with NW-SE trend activating mainly NW-SE normal faults (extensional stage), and strike slip with normal component. The strain field 2 is defined by  $e_y$  with NE-SW trend, activating mainly normal faults with NE-SW trend and strike-slip faults under an extensional stage. Colours of the fault planes on the stereograms are related to the type of faults: blue for normal faults, and grey for strike-slip and reds for reverse faults. The red arrow indicates the orientation of  $e_y$ . Blue teeth line is normal faults, red teeth line is reverse faults and grey lines are strike-slips with the sense of movement. Theoretical fault symmetry in each set is also included. (For interpretation of the references to colour in this figure legend, the reader is referred to the Web version of this article.)



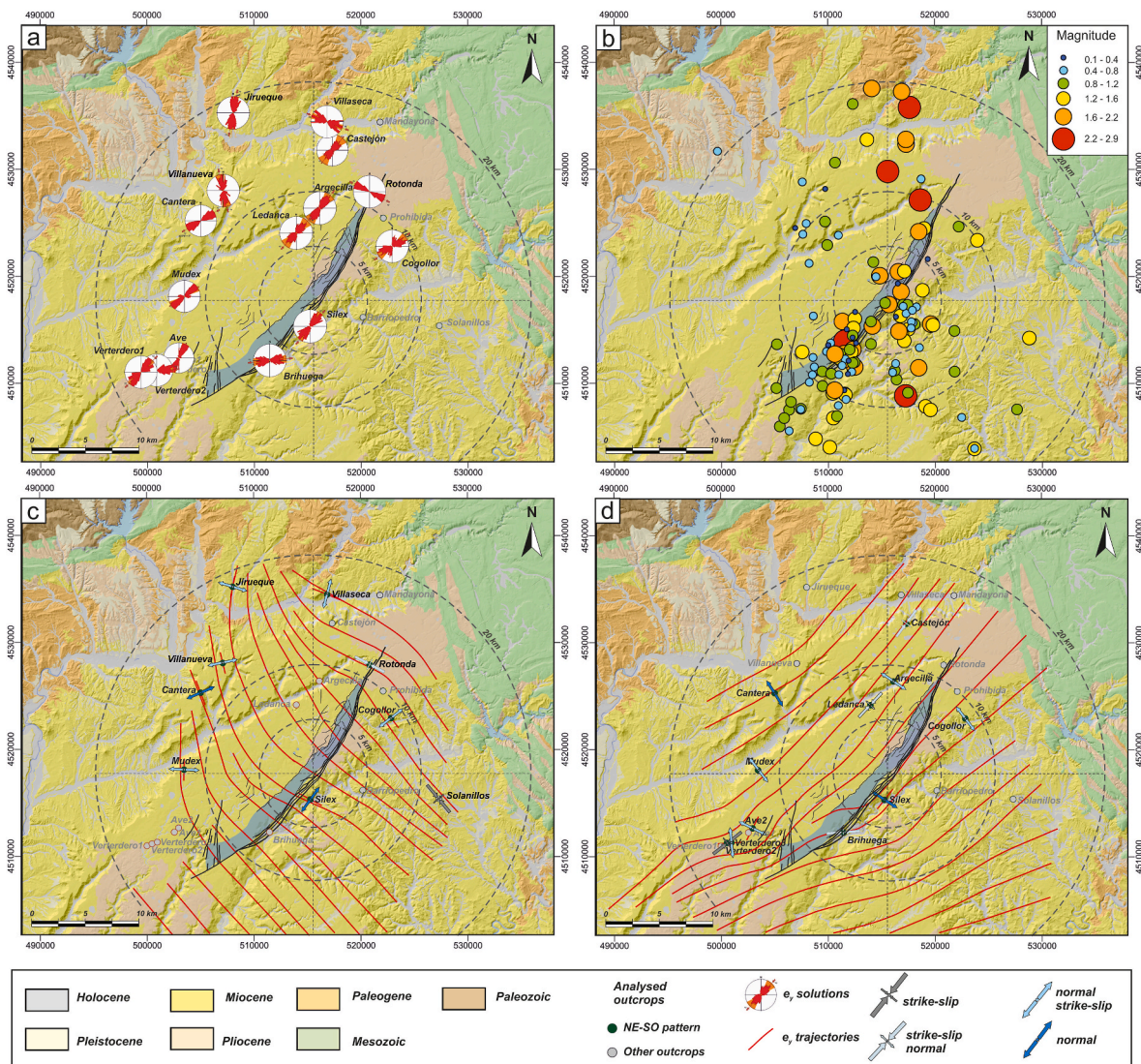


**Fig. 3.** Results of the  $e_y$  trend (3a). Outcrops in grey colour were rejected from the strain analysis (number of data lesser than 5). Spatial distribution of induced earthquakes (3b), taken from the IGN database ([www.ign.es](http://www.ign.es), last access February 2022). The size and colour of the circle is the earthquake magnitude interval. Strain trajectories obtained by using the Lissage software (Lee and Angelier, 1994), according to the strain tensor 1 defined by  $e_y$  with NW-SE trend (3c), and strain tensor 2 defined by  $e_y$  with NE-SE trend (3d). The NE-SW elongated grey polygon represents the structural trap in depth (in which the natural gas is stored) affected by NE-SW to N-S faults, below the Cenozoic sediments. (For interpretation of the references to colour in this figure legend, the reader is referred to the Web version of this article.)

middle Miocene, late Miocene, Pliocene and Quaternary.

#### 4.1. Strain Slip Model and right-dihedral

Most of the outcrops are located on Miocene deposits, mainly limestone, dolomite and marls (Fig. 3a). Two strain fields have been interpreted (Fig. 2, see supplementary material for results: Right Dihedral, Slip Method and K'-diagram). A first strain field is defined by  $e_y$  with NW-SE trend and two components (Fig. 2): 1a) extensional component defined by normal faults with NW-SE trend, and 1b) compressional component activating strike-slip faults with reverse component, oriented NNE-SSW and NNW-SSE. The second strain field is defined by  $e_y$  with NE-SW trend and exhibits two components: 2a) extensional component defined by normal faults with NE-SW trend, and 2b) compressional component is only defined by a few ENE-WSW strike-slip faults ( $n = 11$ , Fig. 2) with reverse component, and N-S faults with reverse component ( $n = 7$ , Fig. 2).

A total of 8 outcrops were removed due to the low quality of the data (Fig. 3a, grey names). 6 outcrops are located within the circle of 10 km of

radius, showing the  $e_y$  with NE-SW trend recorded by late Miocene rocks. (Fig. 3a). 9 outcrops are located within the 20 km radius circle,  $e_y$  with NE-SW trend under an extensional strain field with strike-slip component. 114 fault-slip data showed results mechanically compatible with a strain tensor oriented NW-SE (strain field 1a), under an extensional regime and with strike-slip component. 162 fault-slip data are congruent with a strain tensor oriented NE-SW under an extensional regime. 32 fault-slip data have shown a strain tensor with  $e_y$  with E-W trend under an extensional regime with strike-slip component. 28 fault-slip data defined a strain tensor with  $e_y$  showing N-S trend.

The horizontal strain trajectories (Fig. 3c and d) were plotted by using the software Lissage (Lee and Angelier, 1994). Strain trajectories for field 1 are slightly curved from a N-S to NW-SE trend. These trajectories are perpendicular to the NE-SW thrust (Fig. 3c) bounding the reservoir to the SE. (Fig. 3c), accommodating strain in the structural trap. Secondary horizontal strain trajectories are parallel to the structural trap (Fig. 3d).

#### 4.2. Induced seismicity

A set of 141 earthquakes were recorded within the 20 km radius circle around the Yela facilities, since the starting date of Yela operations in 2012 up to 2021 ([www.ign.es](http://www.ign.es), last access February 2022, Fig. 3. See supplementary information). Instrumental data recorded before 2012 show four earthquakes (two in 1982 of magnitude  $M = 4.1$  and  $M = 2.9$ , one in 1996 of  $M = 2.8$ , and other in 2001 with magnitude = 2.5). No micro earthquakes ( $M < 2$ ) have been recorded in the zone before the geologic gas storage was operational.

The geological natural gas storage facility at Yela is commonly defined in the term of energy storage, using the physical units kWh (to check monthly gas energy storage, see the official web browser at [https://www.enagas.es/enagas/es/Transporte\\_de\\_gas/Almacenamientos\\_Subterranos](https://www.enagas.es/enagas/es/Transporte_de_gas/Almacenamientos_Subterranos), last access February 2022). Data of gas operations used in this work were obtained from this official web site. To represent volume gas data, we have changed from energy units (kWh) to volume units ( $m^3$ ) applying the following equation:

$$\text{Energy (kWh)} = [\text{vol (m}^3\text{)} * \text{calorific value (MJ/m}^3\text{)} * 1.02264] / 3.6 \text{ equation [1]}$$

The calorific value of natural gas, the amount of heat produced on combusting a unit volume of gas, usually ranges between 37.5 and 43 MJ/ $m^3$ , and depending on the quality of natural gas, it can deviate  $\pm 5\%$ . 1.02264 is a constant correction factor, and 3.6 is the conversion factor for kWh. However, without more than a 5% loss in accuracy, we assume that 1  $m^3$  of natural gas corresponds to 10.55 kWh.

Plotting the monthly seismic energy (J) released with the injection/

withdrawal gas volume ( $m^3$ ) into the reservoir (Fig. 4a and b), the injection maximum volume is shown in the summer season, while the gas maximum withdrawal volume in autumn-winter seasons. The gas operations (Fig. 4c) shows a starting point in 2012, related with a cluster of 21 earthquakes with a maximum magnitude of  $M = 2$  (see left circle in Fig. 4c). The maximum cluster comprises 43 earthquakes of maximum magnitude of  $M = 2.3$ , which occurred in October 2017 (Fig. 4). The gas storage worked at his maximum capacity from May 2019 to present day, showing a typical seasonal saw-curve of injection/withdrawal (Fig. 4c, right grey shadow zone).

The gas injection/withdrawal operation has been increasing from 2012 to July 2021, according to the maximum stored gas into the reservoir (Fig. 4a). We have classified the seismic peaks between the years 2012 and 2021 (Fig. 4c). The first peak (P12a) is related with the starting operations in Yela, in March of 2012, with an earthquake of  $M = 2.3$  at 11 km depth, although no data about injection/withdrawal volume are available. The second injection peak of 2012 (P12b, November, Fig. 4b) triggered 13 earthquakes with  $M_{\text{max}} = 2.1$ , between November and early December 2012. Most of the earthquake peaks are related to the injection stages, either displaced with a time lag from the annual maximum injection date (see arrows in Fig. 4a), or in coincidence with the month of the maximum injection volume. No relationship between gas withdrawal and earthquake has been established (Fig. 4b).

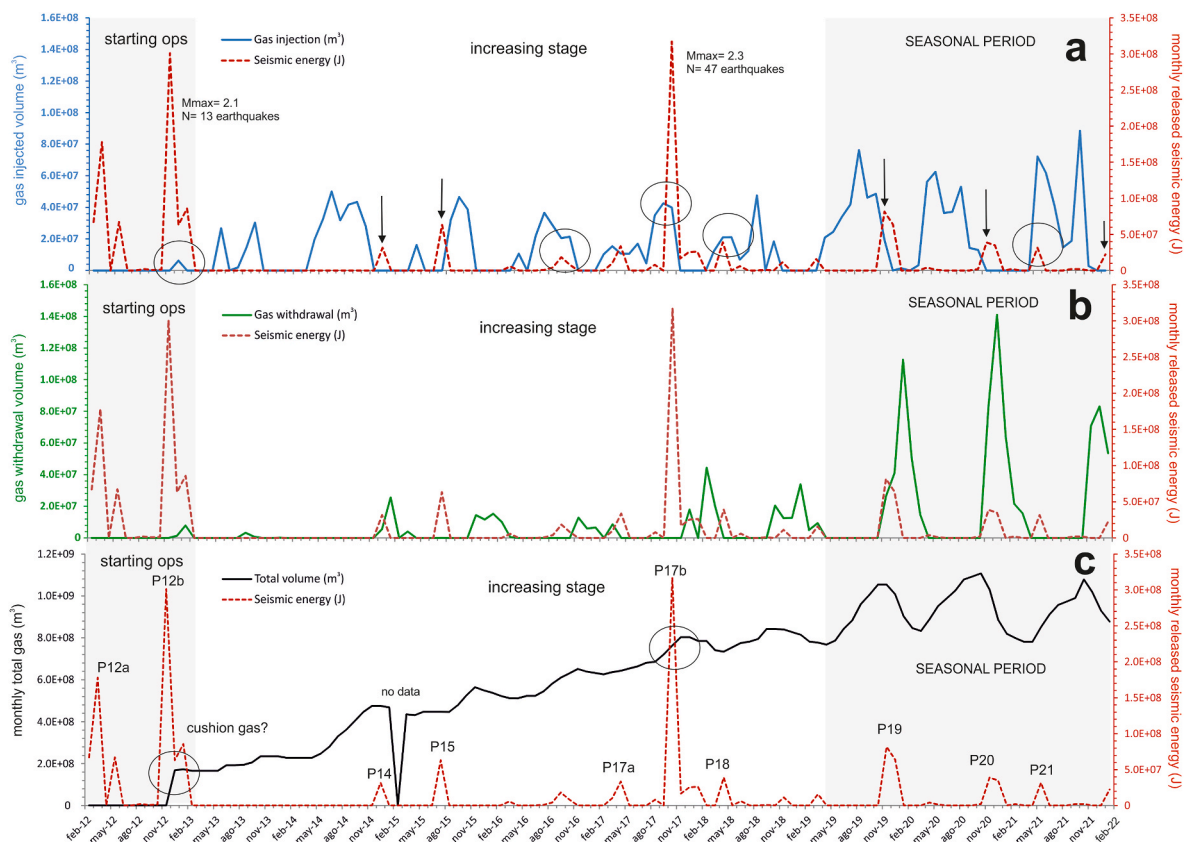


**Fig. 4.** Seismic energy released (red line in joules) from February 2012 to January 2022, and gas operations in Yela gas storage site. **4a.** injection volume in blue line, with arrows showing the temporal relationship between maximum injection date and earthquake occurrence in a time lag and circles when injection and earthquake are in the same month. **4b.** Withdrawal volume in green line. **4c.** Comparison between the seismic energy released (red line) and total stored gas (black line, in  $m^3$ ). P# represents classified seismic peaks by year. Grey shadow zones are the starting operations time interval (left) and the seasonal storage operations (right). Circle indicates the maximum earthquake occurrence. (For interpretation of the references to colour in this figure legend, the reader is referred to the Web version of this article.)



## 5. Discussion

### 5.1. Strain/stress field

10 focal mechanism solutions were used (Fig. 5, Herraiz et al., 2000; Giner-Robles et al., 2012, **supplementary material, excel file earthquakes**). Most of them are located south of the Yela site related to the basement flexural structure (Giner-Robles et al., 2012) and are in agreement with the regional strain field defined by Herraiz et al. (2000). Reverse earthquakes focal mechanisms reveal a compressive stage in the Madrid Basin.

The strain field defined by the  $e_y$  orientation and obtained from the slip-method and the right-dihedral are in agreement in comparison with the seismic regional strain field obtained from the analysis of the focal mechanism solutions (Fig. 5,  $e_y$  with NW-SW trend and reverse component). The strain field 1, featured by  $e_y$  oriented NW-SE, shows an unambiguously similarity to the  $e_y$  orientation obtained from the focal mechanisms, i.e. N141° versus N139° respectively. 25 fault-slip data agree with the focal mechanism solutions for a regional compressive strain field. Conversely, the K'-diagram shows that the strain field 1 consists of an extensional tectonic strain field (**supplementary material, results-stations.pdf**). The strain field 2 is defined by  $e_y$  N51°, versus  $e_y$  N43° obtained from earthquake focal mechanisms (Fig. 5). This strain field is also compatible with the regional strain field defined by Herraiz et al. (2000), but with extensional component. In both cases, the kinematics comparison between strain fault-slip data and earthquake focal mechanisms are in agreement from the horizontal axes comparison and tectonic regime. Nevertheless, the fault-slip kinematics suggests a local strain field with similar  $e_y$  orientation (strain field 1, NW-SE, Fig. 5), but characterized by extension. Moreover, the secondary

strain field (2) shows a switch of the strain axes, with  $e_y$  oriented NE-SW, perpendicular to strain field 1, and with an extensional component. This interchange of axes could be interpreted as the 3D strain field distribution according to the structure folding. Once the anticline affecting Cretaceous carbonates is formed, the fold core experiences compression, while the upper part undergoes extension (see Fig. 21.18 in Ramsay and Huber, 1987). Therefore, we interpret that the local strain field featured by extension is a shallow strain field (probably less than 5 km deep), where NE-SW and NW-SE faults are reactivated as normal faults. Both fault sets configure a 3D arrangement of extensional structures prone to leak fluid by lateral migration due to overpressure..

The stress field obtained from the Delvaux analysis (Fig. 6) is defined as a reverse stress field featured by  $\sigma_1$  with N136° (NW-SE) trend,  $\sigma_3$  vertical, and  $\sigma_2$  with N41° (NE-SW) trend. This result is in agreement with the results obtained from the fault-slip data and the orientation of  $e_y$  (ranging between N 119°–141°, Fig. 2). The result of the dilatation tendency indicates that faults oriented NNE-SSW and NE-SW could be reactivated as reverse faults (Fig. 6). Therefore, there is a coincidence between the  $e_y$  orientation (strain field), and the  $\sigma_1$  orientation (stress field) defined by the focal mechanism solutions from regional earthquakes and the fault-slip data measured in the nearby outcrops. This trend is NW-SE, in agreement with the regional active stress field defined by Herraiz et al. (2000).

### 5.2. Induced seismicity

The first injection gas operation triggered induced seismicity in November 2012 (Fig. 4b, P12a and P12b), probably related to the increasing of the pore pressure. However, the next injection stages in November 2013, 2014, 2015 and 2016 triggered a few earthquakes not

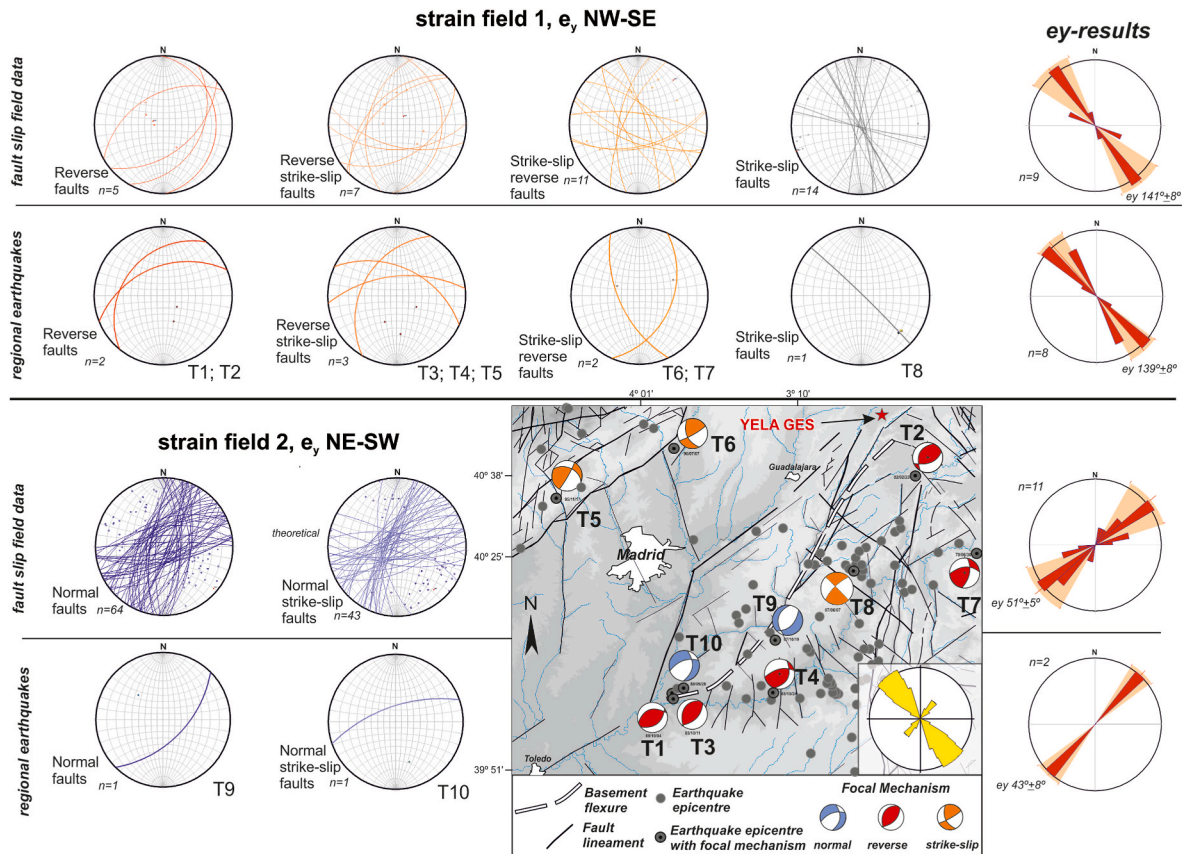


**Fig. 5.** Comparison between the fault planes and nodal planes of the focal mechanism solutions in each strain field with the  $e_y$  direction obtained from the kinematic analysis. Location of the map in Fig. 1b. The yellow rose diagram is the total regional result of  $e_y$  from earthquakes. Flexure dashed line indicates basement flexure according to Giner-Robles et al. (2012). (For interpretation of the references to colour in this figure legend, the reader is referred to the Web version of this article.)



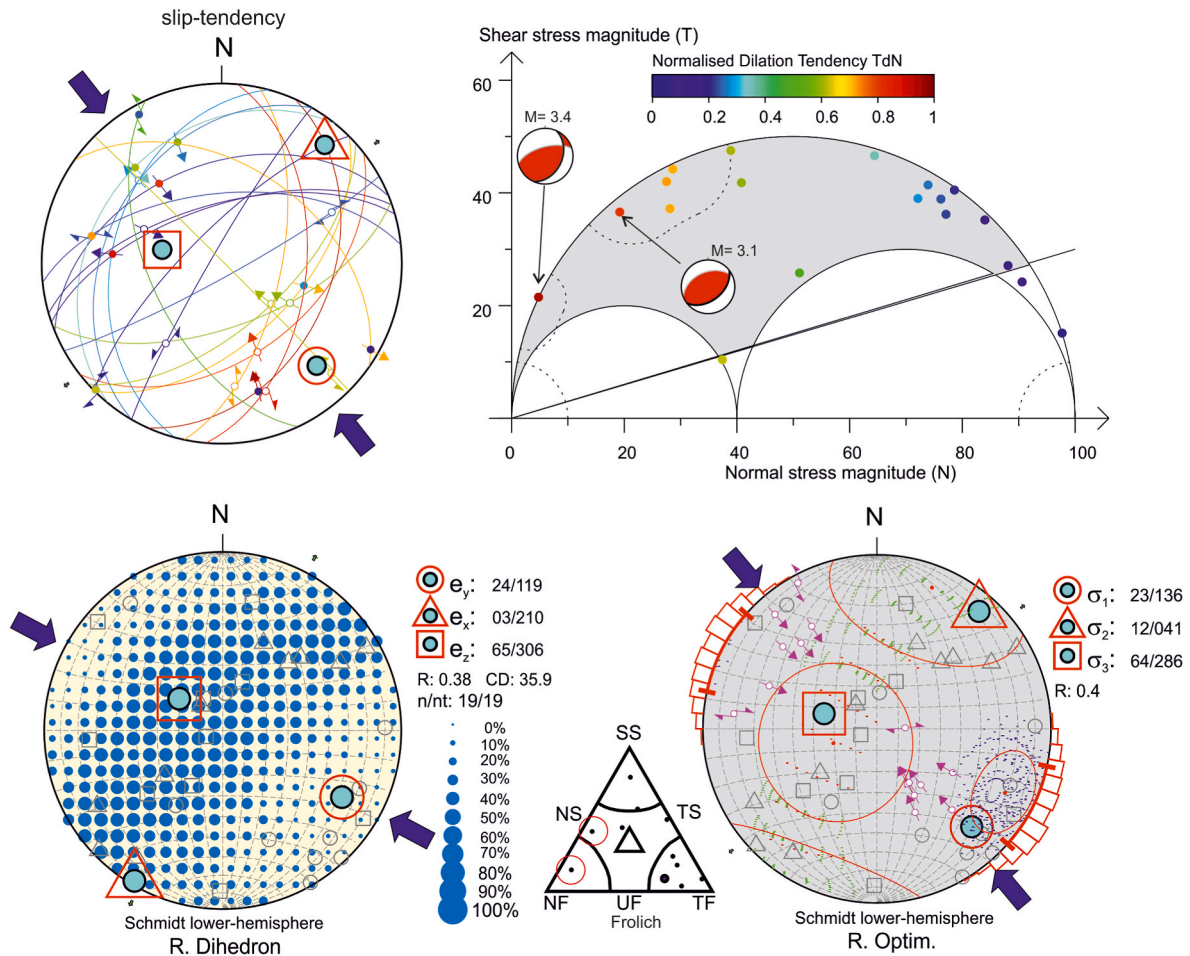


**Fig. 6.** Stress field obtained from the focal mechanism solutions and comparative with the strain field from the Delvaux software. Slip-tendency analysis shows active planes for reverse faults with NNE-SSW and NE-SW trend, and dipping SE.

larger than  $M = 2$  (occurred in July 2015, event P15, in coincidence with summer injection operation). The accumulated gas in this period was about  $4.7 \times 10^6 \text{ m}^3$ . During November 2017, the induced seismicity notably increased (Fig. 4b, P17b) with 47 earthquakes and a maximum magnitude of  $M_{\text{max}} = 2.3$ . This cluster shows up when the total stored gas volume reaches approximately  $7.6 \times 10^8 \text{ m}^3$  (Fig. 4b). From 2017 to June 2021, two decreasing seismic peaks (magnitude and energy, P19, P20) were detected in November 2019 and 2020. Both peaks coincide with the accumulated underground energy (Fig. 4b), related with the injection/withdrawal balance (remaining stored gas, injected gas minus withdrawn gas). Our results suggest that small induced seismic peaks appear (P12, P14, P17b, P19, P20, Fig. 4) due to winter operations (between November and February). To reinforce this, we have applied a cross correlation analysis between the injection data and earthquake occurrence (see supplementary material, correlation.pdf). Both time series reveal stationarity and the correlation shows a lag of 3 months between the injection and the earthquake occurrence, which takes place at the end of the injection operations. Therefore, we interpret that micro-earthquakes are triggered when the maximum reservoir pore pressure is reached at the end of the injection operations. Delayed triggering of induced earthquake is nowadays a matter of discussion (e. g. Peña-Castro et al., 2019; Gao et al., 2022; Lasocki et al., 2022). The study of this delay time is far beyond the objective of this work.

On the other hand, the depth distribution of the induced earthquake hypocentres (20 km away from Yela) shows a maximum between 3 and 6 km (Fig. 7). Three of the regional earthquakes (50 km away of Yela) are located at 2 km depth (plus error bar, see the vertical red line in Fig. 7), which are defined as reverse earthquakes with strike-slip

component (Giner-Robles et al., 2012). This suggests that the Yela reservoir (2,300 m depth) is affected by the regional reverse strain field. Therefore, reverse earthquakes could be affecting the reservoir, along with normal earthquakes related to the local extensional strain field. The sense of relaxation during the local seismic event is a function of the orientation and the resolved stress along such failure planes.

Regarding the potential induced maximum earthquake magnitude, we have applied the McGarr empirical equation (McGarr, 2014, equation 13):

$$M_{0\text{max}} = G \cdot \Delta V \quad \text{Equation [2]}$$

Where  $M_{0\text{max}}$  is the maximum seismic moment,  $\Delta V$  is the injected gas, and  $G$  is the modulus of rigidity and normally used  $= 30 \text{ GPa}$ . In Yela, the maximum volume of stored gas was estimated around  $1.14 \times 10^9 \text{ m}^3$  of gas volume (see <https://www.enagas.es/stfls/EnagasImport/Ficheros/513/97/Folleto%20Yela%20-%20Ingl%C3%A9s.pdf> last access August 2021), corresponding to  $1.2 \times 10^{10} \text{ kWh}$  of energy storage. Besides, future induced seismicity clusters could be related with a rapid daily flow injection, instead of the total stored volume. According to the technical disposals of the Yela, the maximum gas flow per day is  $15 \times 10^6 \text{ m}^3/\text{day}$  ( $1.75 \times 10^8 \text{ kWh}$  of officially energy storage).

Applying the McGarr's equation (cushion gas not included), the result is a seismic energy ( $E$ ) of  $1.71 \times 10^{15} \text{ J}$ , which is as minimum magnitude as of  $M 6.5$  ( $\log E = 5.24 + 1.44 \cdot M$ ). However, the magnitude obtained from the application of the McGarr's equation is based on the assumption that all of the strain induced by injecting a fluid is released as a seismic-sourced. However, the reservoir permeability

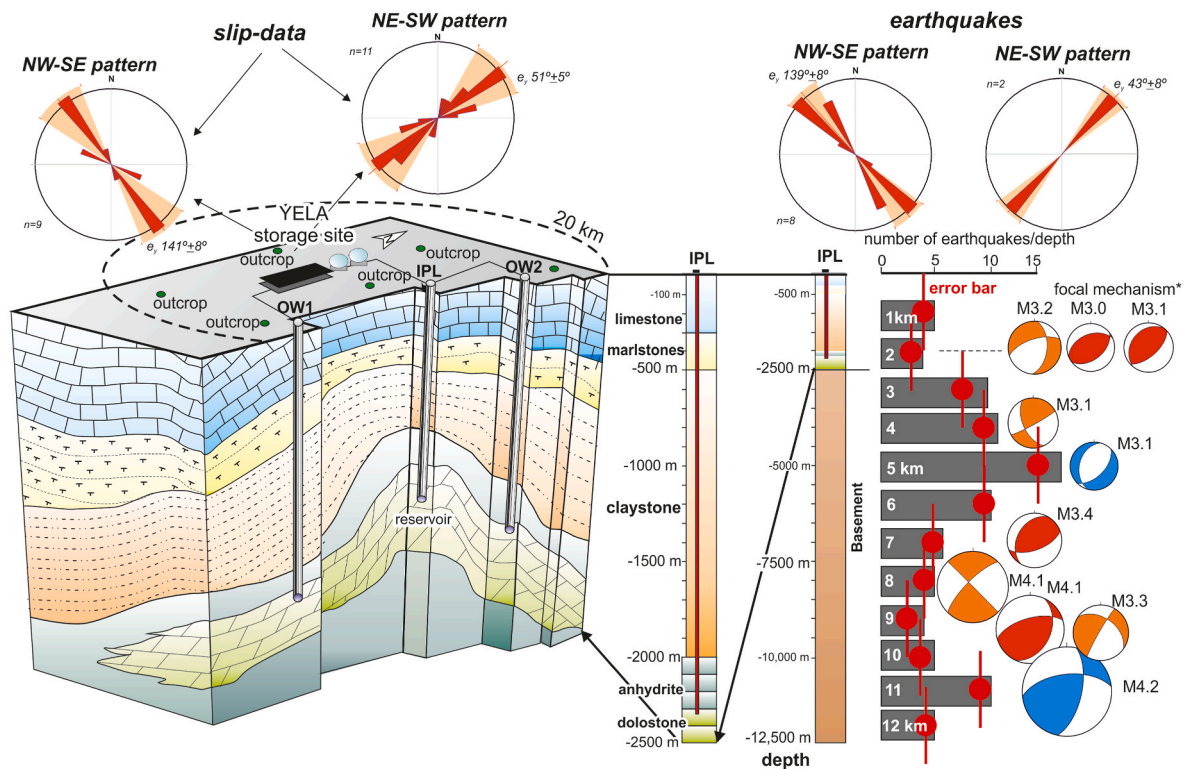


**Fig. 7.** 3D geological sketch of the Yela geological gas storage with the main lithology involved and strain results ( $e_y$  orientation) obtained from the kinematics fault-slip and focal mechanism analysis. The geologic reservoir is located at 2,300 m depth in Cretaceous dolostones. The maximum number of induced earthquakes is located between 4 and 5 km depth (vertical red lines are the error bars). Earthquake Focal mechanism are plotted in depth with their magnitude and solution, red reverse focal mechanism, blue normal mechanism, and orange strike-slip with reverse component. IW, injection well; OW: observation well. Earthquake focal mechanisms obtained from Herraiz et al. (2000) and Giner-Robles et al. (2012) (see supplementary material). 3D geological sketch modified from <https://www.enagas.es/stfls/EnagasImport/Ficheros/513/97/Folleto%20Yela%20-%20Ing%20C3%A9s.pdf> (last access August 2021). (For interpretation of the references to colour in this figure legend, the reader is referred to the Web version of this article.)

allows accommodating the fluid injection with a small variation of the pore pressure, showing creep deformation and heat conductivity. Accordingly, induced earthquakes magnitudes use to be lower than the maximum magnitude obtained from McGarr's equation, which has to be considered as an extreme theoretical approach, rather than the expected earthquake magnitude.

## 6. Conclusions

The regional strain field in the Yela geologic gas storage (central Spain) is defined by a compressive regime with  $e_y$  horizontal shortening trending NW-SE. The regional stress field obtained from the Delvaux fault-slip analysis is reverse and defined by  $\sigma_1$  with NW-SE trend. According to the Slip-Tendency analysis, NE-SW and NNE-SSW oriented fault planes can be reactivated as reverse faults with a strike-slip component. Shallow reverse earthquakes (2 km depth) could occur into the reservoir, as suggested by the regional and local strain and stress fields.

The local strain field shows two extensional solutions defined by  $e_y$  NW-SE (strain field 1) and  $e_y$  NE-SW trend (strain field 2). These local strain induced the reactivation of faults oriented NW-SE as normal faults and N-S faults as strike-slip faults. Lateral underground gas leakage would be determined by normal NW-SE faults, and N-S/E-W strike-slip faults with an extensional component.

Induced seismicity related to Yela operations was recorded in the time period comprised between 2012 and 2021. Initially, a seismic cluster was related to the starting injection operations. Then, different seasonally seismic peaks were identified in summer operations, during the injection phase, but it decreases in frequency and earthquake magnitude year by year. A time lag of 3 months has been determined

from cross correlation analysis. A seismic cluster with 47 earthquakes and with a  $M_{\max} = 2.3$  took place during the summer-autumn operations of 2017. Ongoing summer operations of injection triggered small clusters of induced seismicity in autumn/winter, although the recorded induced earthquake activities have decreased in frequency and magnitude over the last period from 2017 to 2021. However, there is no model to explain this fact despite the relationship between injection gas and earthquake occurrence is positive. Since Yela is working at the maximum stored gas volume ( $1.1 \cdot 10^9 \text{ m}^3$ ) at present day, future relevant and potentially felt earthquake clusters of induced seismicity could be related to the rapid daily injection gas of the reservoir instead of the maximum volume storage.

## Declaration of competing interest

The authors declare the following financial interests/personal relationships which may be considered as potential competing interests.

This work was partially funded by ENAGAS S.A., the Spanish energy company managing YELA AS underground energy storage

## Acknowledgements

In memoriam of Professor John Graham Ramsay, who inspired us to study structural geology and apply his pioneering research in the study of the brittle deformation, fault kinematics and earthquakes. This work has been funded by ENAGAS S.A. and partially funded by the project FAMRAD PID2020-113407RB-I00, Spanish Ministry of Science and Innovation and EU – FEDER. We wish to thank Pr. Damien Delvaux for the free use of the Win-Tensor v. 5.9.2 software, downloaded at [http://damiendelvaux.be/Tensor/WinTensor/win-tensor\\_download.html](http://damiendelvaux.be/Tensor/WinTensor/win-tensor_download.html). The

authors would also like to thank four anonymous reviewers who provided helpful revisions that improved the manuscript.

## Appendix A. Supplementary data

Supplementary data to this article can be found online at <https://doi.org/10.1016/j.jsg.2022.104662>.

## References

- Anderson, E.M., 1951. *The Dynamics of Faulting and Dyke Formation with Application to Britain*, second ed. Oliver and Boyd, Edinburgh, p. 206.
- Angelier, J., 1990. Inversion of field data in fault tectonics to obtain the regional stress-III. A new rapid direct inversion method by analytical means. *Geophys. J. Int.* 103, 363–376. <https://doi.org/10.1111/j.1365-246X.1990.tb01777.x>.
- Angelier, J., Mechler, P., 1977. Sur une méthode graphique de recherche des contraintes principales également utilisable en tectonique et en sismologie: la méthode des dièdres droits. *Bull. Soc. Geol. Fr.* 19, 1309–1318. <https://doi.org/10.2113/gssgfbull.S7-XIX.6.1309>.
- Amrouch, K., Lacombe, O., Bellahsen, N., Daniel, J.-M., Callot, J.-P., 2010. Stress and strain patterns, kinematics and deformation mechanisms in a basement-cored anticline: sheep Mountain Anticline, Wyoming. *Tectonics* 29. <https://doi.org/10.1029/2009TC002525>. TC1005.
- Álvarez-Gómez, J.A., 2019. FMC — earthquake focal mechanisms data management, cluster and classification. *SoftwareX* 9, 299–307. <https://doi.org/10.1016/j.softx.2019.03.008>.
- Armijo, R., Carey, E., Cisternas, A., 1982. The inverse problem in microtectonics and the separation of tectonic phases. *Tectonophysics* 82, 145–160. [https://doi.org/10.1016/0040-1951\(82\)90092-0](https://doi.org/10.1016/0040-1951(82)90092-0).
- Capote, R., de Vicente, G., González-Casado, J.M., 1991. An application of the slip model of brittle deformations to focal mechanism analysis in three different plate tectonics situations. *Tectonophysics* 191, 339–409. [https://doi.org/10.1016/0040-1951\(91\)90070-9](https://doi.org/10.1016/0040-1951(91)90070-9).
- Cloetingh, S., Burov, E., Beekman, F., Andeweg, B., Andriessen, P.A.M., García-Castellanos, D., de Vicente, G., Vegas, R., 2002. Lithospheric folding in Iberia. *Tectonics* 21. <https://doi.org/10.1029/2001TC901031>, 5–15–26.
- Delvaux, D., Sperner, B., 2003. New aspects of tectonic stress inversion with reference to the TENSOR program. *Geol. Soc. Lond. Special Publ.* 212, 75–100. <https://doi.org/10.1144/GSL.SP.2003.212.01.06>.
- de Vicente, G., Muñoz-Martín, A., 2013. The Madrid Basin and the Central System: a tectonostratigraphic analysis from 2D seismic lines. *Tectonophysics* 602, 259–285. <https://doi.org/10.1016/j.tecto.2012.04.003>.
- de Vicente, G., Vegas, R., Muñoz Martín, A., Silva, P.G., Andriessen, P., Cloetingh, S., González Casado, J.M., Van Wees, J.D., Álvarez, J., Carbo, A., Olaiz, A., 2007. Cenozoic thick-skinned deformation and topography evolution of the Spanish Central System. *Global Planet. Change* 58, 335–381. <https://doi.org/10.1016/j.gloplacha.2006.11.042>.
- Etchecopar, A., Vasseur, G., Daignieres, M., 1981. An inverse problem in microtectonics for the determination of stress tensor from fault striation analysis. *J. Struct. Geol.* 3, 51–65. [https://doi.org/10.1016/0191-8141\(81\)90056-0](https://doi.org/10.1016/0191-8141(81)90056-0).
- Gao, D., Kao, H., Wang, B., Visser, R., Schultz, R., Harrington, R., 2022. Complex 3D migration and delayed triggering of hydraulic fracturing-induced seismicity: a case study near Fox Creek, Alberta. *Geophys. Res. Lett.* 49. <https://doi.org/10.1029/2021GL093979> e2021GL093979.
- Giner-Robles, J.L., Pérez-López, R., Silva, P.G., Jiménez-Díaz, A., Rodríguez-Pascua, M. A., 2012. Recent tectonic model for the upper tagus basin (central Spain). *J. Iber. Geol.* 38 (1), 113–125. [https://doi.org/10.5209/rev\\_JIGE.2012.v38.n1.39208](https://doi.org/10.5209/rev_JIGE.2012.v38.n1.39208).
- Guimerà, J., Mas, R., Alonso, Á., 2004. Intraplate deformation in the NW Iberian Chain: Mesozoic extension and tertiary contractional inversion. *J. Geol. Soc.* 161, 291–303. <https://doi.org/10.1144/0016-764903-055>.
- Herraz, M., De Vicente, G., Lindo-Naupari, R., Giner, J., Simón, J.L., González-Casado, J. M., Vadillo, O., Rodríguez-Pascua, M.A., Cicuéndez, J.I., Casas, A., Cabañas, L., Rincón, P., Cortés, A.L., Ramírez, M., Lucini, M., 2000. The recent (upper Miocene to Quaternary) and present tectonic stress distributions in the Iberian Peninsula. *Tectonics* 19, 762–786. <https://doi.org/10.1029/2000TC900006>.
- Kaverina, A.N., Lander, A.V., Prozorov, A.G., 1996. Global creep distribution and its relation to earthquake-source geometry and tectonic origin. *Geophys. J. Int.* 125, 249–265. <https://doi.org/10.1111/j.1365-246X.1996.tb06549.x>.
- Lacombe, O., 2007. Comparison of paleostress magnitudes from calcite twins with contemporary stress magnitudes and frictional sliding criteria in the continental crust: mechanical implications. *J. Struct. Geol.* 29, 86–99. <https://doi.org/10.1016/j.jsg.2006.08.009>.
- Lasocki, S., Rudziński, Ł., Tokarski, A.K., Orlecka-Sikora, B.A., 2022. Hydrofracturing-triggered earthquake occurred three years after the stimulation. *Energies* 15, 336. <https://doi.org/10.3390/en15010336>.
- Lee, J.C., Angelier, J., 1994. Paleostress trajectory maps based on the results of local determinations: the “lissage” program. *Comput. Geosci.* 20 (2), 161–191. [https://doi.org/10.1016/0098-3004\(94\)90004-3](https://doi.org/10.1016/0098-3004(94)90004-3).
- McGarr, A., 2014. Maximum magnitude earthquakes induced by fluid injection. *J. Geophys. Res.* 119, 1008–1019. <https://doi.org/10.1002/2013JB010597>.
- Pan, P., Wu, Z., Feng, X., Yan, F., 2016. Geomechanical modeling of CO<sub>2</sub> geological storage: a review. *J. Rock Mech. Geotech. Eng.* 8 (6), 936–947. <https://doi.org/10.1016/j.jrmge.2016.10.002>.
- Peña Castro, A.F., Dougherty, S.L., Harrington, R.M., Cochran, E.S., 2019. Delayed dynamic triggering of disposal-induced earthquakes observed by a dense array in northern Oklahoma. *J. Geophys. Res. Solid Earth* 124 (4), 3766–3781. <https://doi.org/10.1029/2018jb017150>.
- Pérez-López, R., Paredes, C., Muñoz-Martín, A., 2005. Relationship between the fractal dimension anisotropy of the spatial faults distribution and the paleostress fields on a Variscan granitic massif (Central Spain): the F-parameter. *J. Struct. Geol.* 27 (4), 663–677. <https://doi.org/10.1016/j.jsg.2005.01.002>.
- Pérez-López, R., Mediato, J.F., Rodríguez-Pascua, M.A., Giner-Robles, J.L., Ramos, A., Martín-Velázquez, S., Martínez-Orio, R., Fernández-Canteli, P., 2020. An active tectonic field for CO<sub>2</sub> storage management: the Hontomín onshore case study (Spain). *Solid Earth* 11, 719–739. <https://doi.org/10.5194/se-11-719-2020>.
- Ramos, A., Fernández, O., Terrinha, P., Muñoz, J.A., 2017. Neogene to recent contraction and basin inversion along the Nubia-Iberia boundary in SW Iberia. *Tectonics* 36, 257–286. <https://doi.org/10.1002/2016TC004262>.
- Ramsay, J.G., 1967. *Folding and Fracturing of Rocks*. McGraw-Hill, New York.
- Ramsay, J.G., Huber, M.I., 1983. *The Techniques of Modern Structural Geology*, 1. Academic Press, London. Strain Analysis.
- Ramsay, J.G., Huber, M.I., 1987. *The Techniques of Modern Structural Geology*, 2. Academic Press, London. Folds and Fractures.
- Reches, Z., 1983. Faulting of rocks in three-dimensional strain fields, II. Theoretical analysis. *Tectonophysics* 95, 133–156. [https://doi.org/10.1016/0040-1951\(83\)90264-0](https://doi.org/10.1016/0040-1951(83)90264-0).
- Reches, Z., 1987. Determination of the tectonic stress tensor from slip along faults that obey the Coulomb yield condition. *Tectonics* 7, 849–861. <https://doi.org/10.1029/TC006i006p00849>.
- Rodríguez, L.R., López, F., Oliveira, J.T., Medialdea, T., Terrinha, P., Matas, J., Martín-Serrano, A., Martín Parra, L.M., Rubio, F., Marín, M., Montes, M., Nozal, F., 2015. Mapa Geológico de la Península Ibérica, Baleares y Canarias a escala 1:1.000.000, edición 2015. IGME, LNEG.
- Scholz, C., 2018. *The seismic cycle*. In: *The Mechanics of Earthquakes and Faulting*, third ed. Cambridge University Press, Cambridge, pp. 228–277.
- Simpson, R.S., 1997. Quantifying Anderson's fault types. *J. Geophys. Res. Solid Earth* 102 (17). <https://doi.org/10.1029/97JB01274>, 909–17,919.
- Verdon, J.P., Stork, A.L., Bissell, R.C., Bond, C.E., Werner, M.J., 2015. Simulation of seismic events induced by CO<sub>2</sub> injection at in Salah, Algeria. *Earth Planet Sci. Lett.* 426, 118–129. <https://doi.org/10.1016/j.epsl.2015.06.029>.
- Wells, D.L., Coppersmith, K.J., 1994. New empirical relationships among magnitude, rupture length, rupture width, rupture area, and surface displacement. *Bull. Seismol. Soc. Am.* 84, 974–1002.
- Žalohar, J., Vrabec, M., 2010. Kinematics and dynamics of fault reactivation: the Cosserat approach. *J. Struct. Geol.* 32, 15–27. <https://doi.org/10.1016/j.jsg.2009.06.008>.